Modification of spin-ice physics in $Ho_2Ti_2O_7$ thin films

Kevin Barry,[1,2] Biwen Zhang,[1,2] Naween Anand,[2,*] Yan Xin,[2] Arturas Vailionis,[3] Jennifer Neu,[1,2] Colin Heikes,[4] Charis Cochran,[2] Haidong Zhou,[2,5] Y. Qiu,[4] William Ratcliff,[4] Theo Siegrist,[2,6] and Christianne Beekman[1,2,†]

[1]*Department of Physics, Florida State University, Tallahassee, Florida 32310, USA*
[2]*National High Magnetic Field Laboratory, Florida State University, Tallahassee, Florida 32310, USA*
[3]*Stanford Nano Shared Facilities, Stanford University, Stanford, California 94305, USA*
[4]*NIST Center for Neutron Research, National Institute of Standards and Technology, Gaithersburg, Maryland 20899, USA*
[5]*Department of Physics and Astronomy, University of Tennessee, Knoxville, Tennessee 37996, USA*
[6]*Department of Chemical and Biomedical Engineering, FAMU-FSU College of Engineering, Tallahassee, Florida 32310, USA*

We present an extensive study on the effect of substrate orientation, strain, stoichiometry, and defects on spin-ice physics in $Ho_2Ti_2O_7$ thin films grown onto yttria-stabilized-zirconia substrates. We find that growth in different orientations produces different strain states in the films. All films exhibit similar c-axis lattice parameters for their relaxed portions, which are consistently larger than the bulk value of 10.1 Å. Transmission electron microscopy reveals antisite disorder and growth defects to be present in the films, but evidence of stuffing is not observed. The amount of disorder depends on the growth orientation, with the (110) film showing the least. Magnetization measurements at 1.8 K show the expected magnetic anisotropy and saturation magnetization values associated with a spin ice for all orientations; shape anisotropy is apparent when comparing in- and out-of-plane directions. Significantly, only the (110)-oriented films display the hallmark spin-ice plateau state in magnetization, albeit less well defined compared to the plateau observed in a single crystal. Neutron-scattering maps on the more disordered (111)-oriented films show the $Q = 0$ phase previously observed in bulk materials, but the $Q = X$ phase giving the plateau state remains elusive. We conclude that the spin-ice physics in thin films is modified by defects and strain, leading to a reduction in the temperature at which correlations drive the system into the spin-ice state.

I. INTRODUCTION

The quest for novel quantum phases that show collective degrees of freedom and fractionalized excitations is one of the central themes in condensed-matter physics. There has been a strong focus recently on geometrically frustrated magnets, which have been shown to host a number of cooperative spin states [1], such as spin-ice and spin-liquid states. The low-temperature state of the spin ice has been characterized as a magnetic Coulomb phase [2–4], a classical spin liquid in which fractionalized excitations (topological defects that behave like magnetic monopoles) have been predicted and experimentally realized [5–7]. Of particular interest are rare-earth pyrochlores that belong to the spin-ice family, such as $Ho_2Ti_2O_7$, which display severe frustration that arises from a combination of the lattice geometry, the sign of the nearest-neighbor magnetic interactions resulting in local ice rules, and a macroscopically degenerate ground state. One important factor determining the ground-state selection in these systems is the single-ion anisotropy [8,9].

$Ho_2Ti_2O_7$ has a cubic structure ($Fd\bar{3}m$ space group) and can be envisioned as Ho^{3+} ions (each with a magnetic moment of $\sim 10\ \mu_B$) residing on a lattice of corner-sharing tetrahedra

[see Fig. 1(a)] [10]. In $Ho_2Ti_2O_7$, the crystal-field doublet ground state results in an Ising-like easy-axis anisotropy [see Fig. 1(b)] with all the spins pointing along the local $\langle 111 \rangle$ axes, i.e., either in or out of the tetrahedra [10,11]. If the system were dominated by antiferromagnetic nearest-neighbor exchange interactions, it would tend to long-range order with an all-in/all-out spin configuration on the tetrahedra. In fact, several theoretical and experimental studies have mostly found antiferromagnetic exchange on geometrically frustrated lattices; however, the first discovery of strong frustration in $Ho_2Ti_2O_7$, a ferromagnetic pyrochlore [12], has challenged our understanding of cooperative magnetic phenomena. The absence of long-range magnetic ordering down to 50 mK in a $Ho_2Ti_2O_7$ bulk crystal [12,13] was confirmed by muon spin relaxation (μSR) and neutron-scattering experiments, but the Curie-Weiss temperature θ_{CW} was estimated to be around 2 K [12–15]. Furthermore, the measurement of the electronic component of magnetic heat capacity [16] has also revealed a broad magnetic peak at around 1.9 K, indicating the buildup of magnetic correlations and removal of magnetic entropy as the system is cooled. Apart from some local spin dynamics [17], this leads to the spins freezing into a state analogous to ice [18,19], a two-in/two-out configuration on the tetrahedra below $T = 0.65$ K [20], while retaining the nonzero Pauling entropy, $S_0 \approx (R/2)\ln(3/2)$, a key thermodynamic characteristic of frustration and the spin-ice state [15,16,18].

———————
*Present address: Argonne National Laboratory, Argonne, Illinois 60439, USA.

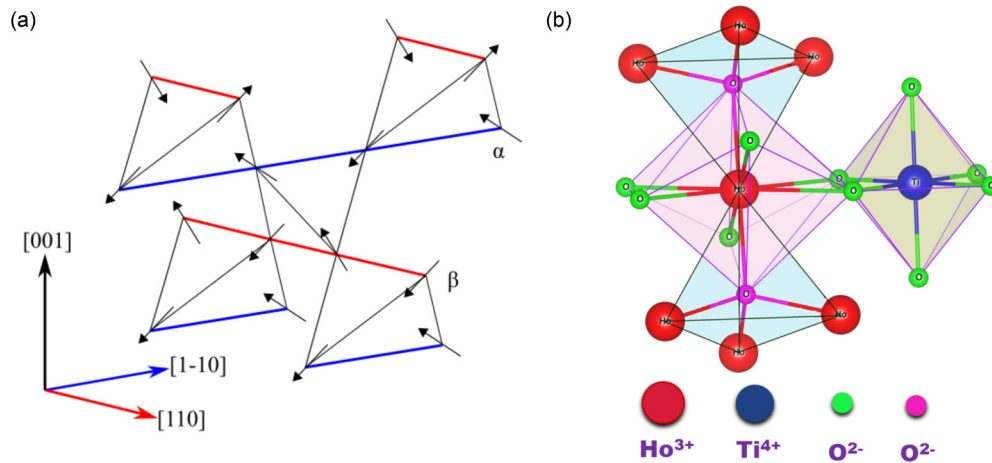†Corresponding author: beekman@magnet.fsu.edu

FIG. 1. (a) Cornersharing tetrahedral network of Ho atoms in an $Ho_2Ti_2O_7$ pyrochlore structure showing a two-in and two-out magnetic configuration. The α and β chains are indicated in blue and red along with their respective crystallographic directions (similar to Ref. [11]). (b) Anisotropic crystal field around an Ho atom leading to two inequivalent oxygen sites (O_1 in a ring around the Ho and O_2 as two apical oxygen atoms along the $\langle 111 \rangle$) and a strong axial symmetry along the $\langle 111 \rangle$ local axis. Red atoms: Ho; blue atoms: Ti; green atoms: O_1; violet atoms: O_2.

As described in [21,22], it is the competition between classical nearest-neighbor dipolar interactions (D_{nn}) and nearest-neighbor quantum superexchange interactions (J_{nn}) that determines the degree of order (or frustration) in the material. As reported by others, a pyrochlore material is a spin ice when $J_{nn}/D_{nn} > -0.91$ and reverts to an unfrustrated ordered antiferromagnetic state for $J_{nn}/D_{nn} < -0.91$ ($Ho_2Ti_2O_7$, $J_{nn}/D_{nn} = -0.27$, $Dy_2Ti_2O_7$, $J_{nn}/D_{nn} = -0.49$) [21,23–25]. Reports on chemical and hydrostatic pressure studies indicate that the magnetic properties and monopole density in pyrochlore single crystals [23,24,26] can be tuned via structural means. Specifically, a tetragonal distortion has been predicted to result in a symmetry-breaking transition out of the Coulomb phase accompanied by a divergence of the susceptibility [27], and uniaxial pressure studies performed on single crystals of $Dy_2Ti_2O_7$ showed that applying pressure along the [001] and [110] crystallographic directions may change the degeneracy of the ground state, inducing a 4% increase in the magnetization at low field and a 1% decrease in magnetization at high field for $P, H \parallel [001]$, in line with predictions [27,28].

Epitaxial strain is usually biaxial and is fundamentally different from hydrostatic and chemical pressure. Therefore, it can be used to lower the local symmetry and to apply an effective transverse field, which should either push the system to a more ordered state or, as predicted in Ref. [29], introduce quantum fluctuations in this otherwise classical system. It is interesting to note that from recent simulations on model spin-ice thin films, it is clear that not only strain, but also confinement, may impact spin-ice physics in thin films. For films with surfaces perpendicular to the [001], the existence of charges at the film surface has been predicted to yield an emergent square ice [30]. While surface charges are predicted for films with (001) surfaces, in films with (110) and (111) surfaces, confinement leads to different behaviors [31]. In other words, rich phase diagrams are expected for strained and confined versions of the spin ice. Experimental studies on thin films of $Dy_2Ti_2O_7$ grown on (110) $Y_2Ti_2O_7$

found evidence of a zero-entropy state at low temperature, suggesting that epitaxial strain can be used to tune the physics of frustrated pyrochlore magnets [32]. A study performed on $Ho_2Ti_2O_7$ thin films grown on yttria-stabilized-zirconia (YSZ) substrates of various orientations showed a plateau in magnetization (similar to behaviors observed in single crystals [15,20,33–35]) when the field is applied along an *in-plane* [111] direction, indicating that spin-ice physics was preserved in those films [36].

In this paper, we present structural and magnetic characterization of a thickness series of high-quality epitaxial thin films of $Ho_2Ti_2O_7$ grown on (111), (001), and (110) YSZ substrates. We find that films grown on different orientations of YSZ lead to different strain states in the films. However, it is important to note that the *relaxed* portion of the films has very similar lattice parameters as extracted from x-ray diffraction (XRD) and transmission electron microscopy (TEM) measurements, regardless of the film orientation and the film thickness. Furthermore, this relaxed lattice parameter is, on average, 0.70% larger than what has been previously reported as the bulk lattice parameter (10.1 Å [37,38]). Several studies have shown that the lattice parameter is quite dependent on the presence of stuffing (replacing Ti^{+4} with Ho^{+3}, taking the system toward $Ho_{2+\delta}Ti_{2-\delta}O_{7-\delta/2}$) [39–44]. To address the questions of stuffing, valence state, and antisite disorder, we have collected TEM images and performed X-ray photoemission spectroscopy (XPS) measurements on our thin-film samples and compared these results to those collected on a single crystal. These measurements indicate the absence of stuffing and the presence of antisite disorder and growth defects within the films; the effect of such defects on spin-ice physics is discussed here. We also present magnetization measurements for all the orientations and find that in-plane and out-of-plane behaviors are different, indicating that the shape anisotropy inherent to thin films affects spin-ice physics. Furthermore, while the hallmark spin-ice plateau is present in a film that has the [111] direction in the plane of the film [for the (110) film], for the films with the [111] direction pointing out of the plane,
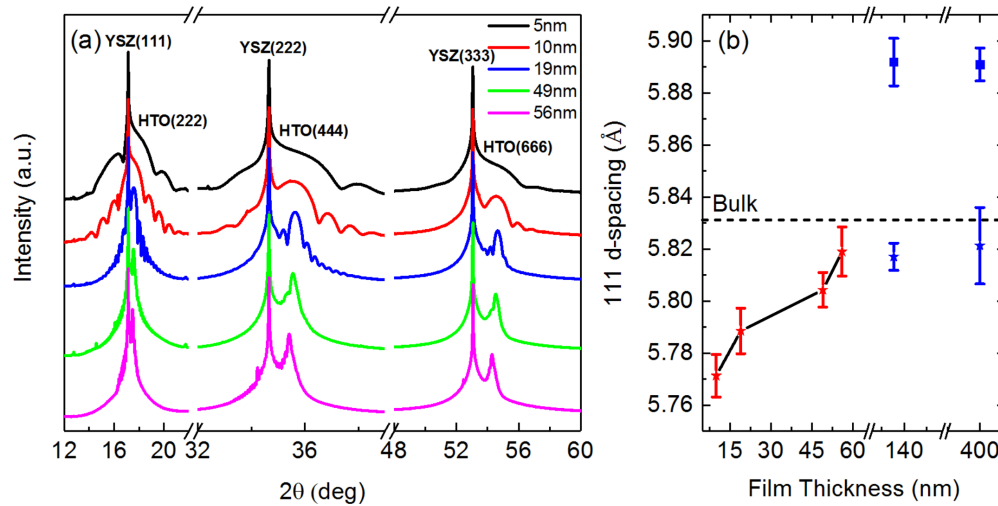
FIG. 2. (a) Synchrotron XRD $\theta - 2\theta$ scans for (111) films ranging in thickness from 5 to 56 nm grown on YSZ substrates showing the (111), (222), and (333) substrate peaks and the (222), (444), and (666) film peaks, which are labeled with HTO. (b) Extracted d spacing along the [111] crystallographic direction as a function of film thickness for the same films shown in (a) (red star symbols). The line is a guide to the eye. The error bars on each point are a result of the standard deviation in the calculated d spacings from each of the visible $\langle 111 \rangle$ film reflections as well as the angular resolution in the measurements (0.01°–0.02°). Also shown are the d spacings for a 132 nm and a 400 nm film grown on (111) YSZ, for both the strained (blue star symbols) and the relaxed (blue square symbols) portions, extracted from laboratory-scale measurements (see Supplemental Material [45] for more information). The error bars were determined based on the fitted FWHM values of the reflections. The d spacing for bulk ($a = 10.1$ Å) is indicated with the dashed line.

the plateau is not observed. The (110) film that shows the hallmark plateau state also has less antisite disorder compared to the other orientations. It has to be noted that the observed magnetization plateau in the (110) film is somewhat washed out at 1.8 K. We rule out misalignment of the field with the [111] direction as a probable cause; hence, we conclude that the spin-ice physics in the (110) films [and presumably in the (111) and (001) films] is modified in that they exhibit a reduction in the temperature at which correlations drive the system into the spin-ice state. The observed antisite disorder and the enlarged unit cell likely play a role.

II. EXPERIMENTAL DETAILS

$Ho_2Ti_2O_7$ epitaxial thin films were grown on (111), (001), and (110) YSZ substrates using pulsed laser deposition (PLD). The laser (KrF excimer, $\lambda = 248$ nm) pulses were focused onto a rotating polycrystalline $Ho_2Ti_2O_7$ stoichiometric target with an energy density of ∼0.5 J/cm² and repetition rate of 4 Hz. The films were grown at an average growth rate of about 0.030 nm/sec in a vacuum system with a base pressure of 1×10^{-7} Torr in a 0.1 Torr oxygen background pressure, while the substrate was kept at a temperature of 800 °C. After deposition, the films were cooled to room temperature at a rate of 10 °C/min in the same background pressure of oxygen. Atomic-force microscopy (AFM) using an Asylum MFP-3D system [46] operated in tapping mode was done on the substrates before growth and on the films after growth (see Supplemental Material [45]). After growth, the surface morphology of the films show the film surfaces to be flat and smooth, with a fine grainy structure and a root-mean-square roughness ∼1 nm, consistent with results

reported by others [36]. Film thicknesses were determined via x-ray reflectivity measurements by fitting the thickness fringes [47] (see Supplemental Material [45]).

The structural characterization of the (111) films with various thicknesses was performed using synchrotron x-ray diffraction at beam line 7-2 of the Stanford Synchrotron Radiation Lightsource (SSRL) [Fig. 2(a)]. Reciprocal space maps (RSMs) on (001), (110), and (111) films were performed using a laboratory-based x-ray diffractometer at the Stanford Nano Shared Facilities at Stanford University. Additional x-ray diffraction measurements (coupled scans) were performed at the National High Magnetic Field Laboratory. XPS spectra were collected on single-crystal and thin-film samples using a PHI 5100 Series XPS spectrometer [46]. XPS measurements were performed using a nonmonochromatic Mg K_α radiation source operated at 300 W with a 180 degree spherical sector analyzer operating at a constant pass energy of 44.75 eV. Measurements were collected at a base pressure of 1×10^{-10} Torr and at a take-off angle of 45°. Neutron-diffraction experiments on the (111) films were performed at the National Institute of Standards and Technology Center for Neutron Research (NIST-NCNR) at the Multi Axis Crystal Spectrometer (MACS) [48] and the Spin Polarized Inelastic Neutron Spectrometer (SPINS) beam lines. Elastic measurements on MACS were made at a fixed neutron energy of 5 meV in double-focusing mode with two cooled Be filters to eliminate higher-order contamination to the beam. SPINS data were collected at a fixed neutron energy of 5 meV in flat analyzer mode using a ³He point detector with dual-cooled Be filters at a collimation of 80'-s-80'. MACS and SPINS data reduction were performed using the DAVE software package [49]. TEM experiments were performed using a JEM-ARM200cF transmission electron microscope [46]. The investigated samples

were prepared with a Gatan Precision Ion Polishing System (PIPS) [46]. Magnetization measurements in an applied field of $H = 1000$ Oe as a function of temperature and as a function of field at fixed temperature were performed in a Quantum Design magnetic properties measurement system (MPMS) [46].

III. RESULTS AND DISCUSSION

The results of the structural characterization done at SSRL are presented in Fig. 2(a), which shows $\theta - 2\theta$ scans near the YSZ (111), (222), and (333) reflections for $Ho_2Ti_2O_7$ thin films grown on (111) YSZ of varying thickness between 5 and 56 nm. Prominent thickness fringes can be observed on all the major film peaks, displaying the high structural quality and thickness uniformity of our films. A trend of decreasing 2θ position with increasing film thickness can be observed for all film reflections, indicating an increase of the out-of-plane (111) d spacing with increasing film thickness [see Fig. 2(b), red symbols]. The d spacing for each film was determined from the (111), (222), (444), and (666) film reflections.

To investigate the strain state of our films, RSMs were measured on films grown on (111), (001), and (110) substrates. The RSMs taken around the (226) diffraction peak of $Ho_2Ti_2O_7$ for a 56 nm (111) and a 50 nm (001) thin film, and around the (662) for a 118 nm (110) thin film, are presented in Figs. 3(a)–3(c). The previously reported lattice parameter of bulk $Ho_2Ti_2O_7$ is 10.1 Å [37,38], while the lattice parameter of YSZ is 5.15 Å as extracted from our synchrotron measurements presented in Fig. 2 and reported by others [50,51]. This yields a lattice mismatch of about 2% between film and substrate (tensile strain) with one $Ho_2Ti_2O_7$ unit cell fitting onto a block of 2×2 YSZ unit cells. We find that for the 56 nm film grown on (111) YSZ, most of the scattering intensity from the film occurs at an in-plane value of the scattering vector matching that of the substrate; in other words, most of this film has in-plane lattice parameters that are matched with the YSZ, i.e., this portion of the film is fully strained. The film does show some signs of strain relaxation, i.e., that the top layer of the film has relaxed (intensity appears at different in-plane q values). The 50 nm (001) film displays a strained interfacial layer, but it is clear that a significant portion of the film exhibits in-plane values for the scattering vector that are distinct from that of the substrate, indicating the presence of considerable relaxation. Here we note that in the previous work done [36], it was found that no intermediate strained layer was observed for a 33 nm (001) film studied. In Fig. 3(c), an RSM around the (662) $Ho_2Ti_2O_7$ reflection of a 118 nm film grown onto (110) YSZ is shown; this RSM does not show evidence of a strained interfacial layer, but only a single presumably fully relaxed film [see Supplemental Material [45] for additional RSMs for a 132 nm (111) film and for a 35 nm (001) film]. In each RSM, we have also shown the position of where the bulk $Ho_2Ti_2O_7$ reflection would occur based on the previously reported lattice parameter of 10.1 Å. It is clear that our films are not relaxing to this previously reported bulk value. Using the q values from films grown on each substrate orientation, we extract lattice parameter values for both the strained and relaxed portions of the films (see Table I and the Supplemental Material for more details [45]). For comparison, in Fig. 2(b) we present the calculated
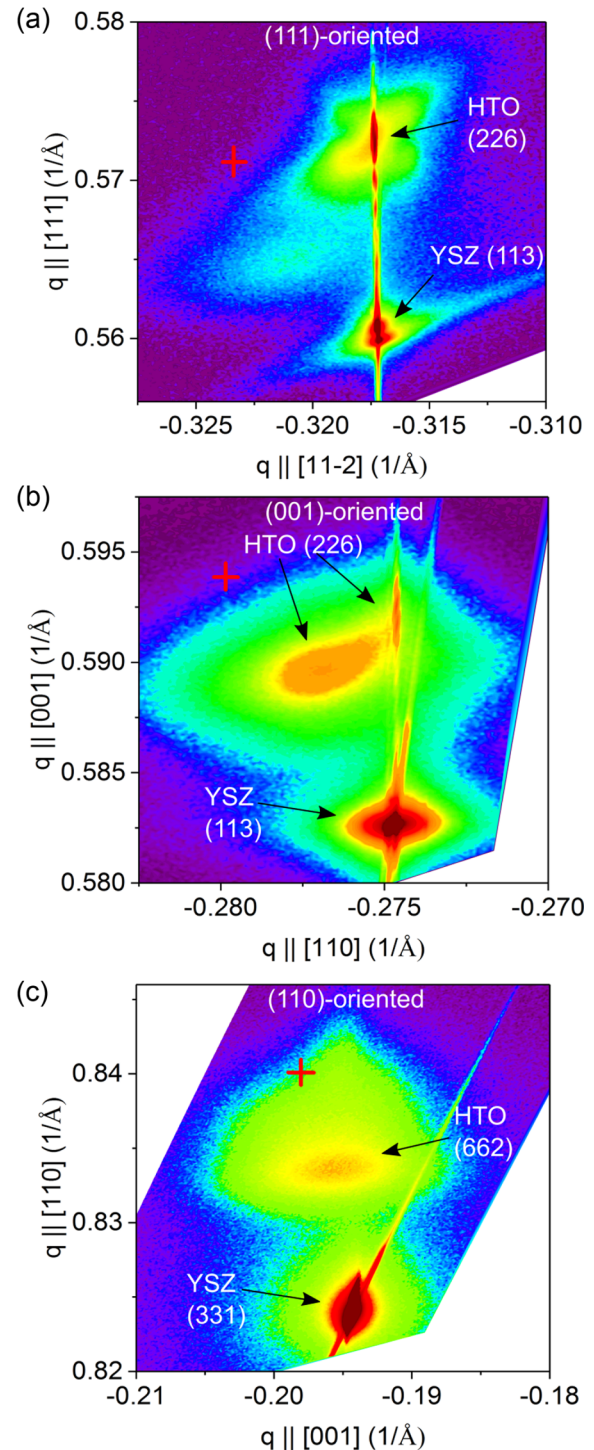

FIG. 3. (a) Reciprocal space map of the (226) diffraction peak of $Ho_2Ti_2O_7$ for a 56-nm-thick film grown on a (111) YSZ substrate. (b) RSM of the (226) diffraction peak of $Ho_2Ti_2O_7$ for a 50-nm-thick film grown on a (001) YSZ substrate. The (113) diffraction peak of YSZ is marked by the intensity at the bottom of each image. (c) RSM of the (662) diffraction peak of $Ho_2Ti_2O_7$ for a 118-nm-thick film grown on a (110) YSZ substrate. The (331) diffraction peak of YSZ is marked by the intensity at the bottom of the image. The red crosshairs indicate the position of bulk $Ho_2Ti_2O_7$ with a lattice parameter of 10.1 Å in each image. The diagonal streaks of intensity across the substrate reflection in (b) and (c) are a result of the finite step size of the one-dimensional detector used for the measurement. The film peaks are indicated with the label HTO.

TABLE I. Lattice constant summary. For the (001) film, the unit cell is tetragonal with the c axis normal to the film plane, while the a axis is in the film plane. For the (110) films, the c axis is an in-plane direction, while the [110] direction points out of the film plane. The lattice parameters for these films were determined from x-ray diffraction [assuming a tetragonal unit cell for the (110) film]. For the (111) film, the c-axis and a-axis parameters are determined from (00l) and (hh0) reflections from the TEM SAED patterns (assuming a tetragonal unit cell) taken some distance removed from the substrate interface; these parameters are likely associated with a partially or fully relaxed region of the film. The error bars were determined based on the FWHM values of the reflections (see Supplemental Material for more details [45]).

Film thickness	Film normal	c (Å) (strained)	c (Å) (relaxed)	a (Å) (strained)	a (Å) (relaxed)
50 nm	[001]	10.13(3)	10.17(2)	10.29(3)	10.21(6)
118 nm	[110]		10.2(2)		10.18(1)
70 nm	[111]	10.15(2)		10.13(6)	

d spacing in the [111] direction for two additional films (blue symbols), as determined from the RSM (for the 132 nm film) and from a coupled scan (for a 400 nm film), both presented in the Supplemental Material [45]. For each film, we show the d spacing for the strained interfacial layer ($d_{[111]} <$ bulk) and for the relaxed portion of the film ($d_{[111]} >$ bulk), both of which are consistent with the other results. The lattice parameters extracted from this analysis are similar to those previously reported for stuffed variants of $Ho_2Ti_2O_7$, when 30% of the Ti^{4+} sites have been replaced with Ho^{3+}[39,40,42–44]. However, these stuffed stoichiometries are reportedly difficult to obtain [39] and have been synthesized previously via a rapid-cooling method from temperatures much higher than that employed in our growth routine.

Selected area electron diffraction (SAED) patterns were collected using a TEM for films grown on each substrate orientation. We find bright and well-resolved diffraction spots in each case. The SAED pattern for a 70 nm (111) film is shown in the Supplemental Material as a typical example [45]. This SAED pattern was used to extract both the a- and c-axis lattice parameters for the (111) film away from the substrate interface. The extraction process is presented in the Supplemental Material [45] and the resulting values are presented in Table I along with lattice parameters extracted from x-ray diffraction. The lattice parameters from SAED are also consistent with an inflated unit cell compared to what has been previously reported for bulk single crystals. For the films grown on (001) YSZ, we can explicitly determine that the unit cell is tetragonal. The films grown on (111) YSZ are rhombohedral, while those grown on (110) YSZ are orthorhombic. Using the values presented in Table I, it was found that the rhombohedral angle deviates from 90° by $\sim +0.2°$ in the (111) case, consistent with the in-plane tensile strain, while in the (110) film, the angle between the $a(b)$ axis and the [110] direction was found to be $\sim$45.1°.

In order to investigate whether these differences in lattice parameter compared to the previously reported bulk value could be due to deviating stoichiometry, or oxygen deficiency,

we have performed XPS measurements to confirm a 1:1 Ho:Ti ratio in our films. The resulting XPS spectra of the Ti $2p$ and Ho $4d$ regions of a $Ho_2Ti_2O_7$ single crystal, a 400 nm (001) thin film, and a 40 nm (111) thin film are presented in Fig. 4. The Ti $2p_{\frac{1}{2}}$ and Ti $2p_{\frac{3}{2}}$ spin-orbital split doublet was clearly observed for both the thin-film and single-crystal samples, and binding energies are similar to those previously reported for TiO_2 [52–55]. The spectral contributions from the Ti $2p_{\frac{1}{2}}$ and Ti $2p_{\frac{3}{2}}$ doublet were quantified utilizing a mixture of Lorentzian and Gaussian curves for fitting. The multiplet split spectra of Ho $4d$ have been observed for the single-crystal and the thin-film samples. In each case, the spectra, while yielding no well-defined peaks, are qualitatively similar to previous measurements reported on holmium oxide with features occurring at similar binding energies to those reported in the range from 200 to 160 eV [56–59]. The different spectral contributions from the Ho $4d$ multiplet structure were determined by fitting six distinct Gaussian peaks to each data set. Observed differences in the binding energies between the single crystal and the thin films for the two regions, though small, can be attributed to different amounts of sample charging during each measurement. The extracted areas from the fitting of the Ti $2p$ and Ho $4d$ peaks as well as their respective sensitivity factors were used to calculate the relative concentrations of Ho and Ti in each sample. The concentrations were found to be Ti: $50.25 \pm 0.35\%$, Ho: $49.75 \pm 0.48\%$ for the single crystal; Ti: $49.75 \pm 0.43\%$, Ho: $50.25 \pm 0.48\%$ for the 400 nm (001) thin film; and Ti: $49.67 \pm 0.33\%$, Ho: $50.33 \pm 0.41\%$ for the 40 nm (111) thin film. Here the error bars on each concentration are derived from the fitting error on each extracted area. Hence, the films look identical to the single crystal, i.e., they show 1:1 Ho:Ti stoichiometry, and the Ti $2p$ peaks are consistent with Ti^{4+} for all measured samples ruling out the mixed valence on the Ti site. A detailed example of the curve fittings and concentration calculations is presented in the Supplemental Material [45].

To further investigate the microstructure of the films, we compare high-angle-annular-dark-field scanning TEM (HAADF-STEM) images of a $Ho_2Ti_2O_7$ single crystal and of films grown on each substrate orientation [(111), (001), and (110)]. Figure 5(a) shows an atomic resolution image of the single crystal, while Figs. 5(b) and 5(c) show images from the 118 nm (110) $Ho_2Ti_2O_7$ film, collected away from and close to the substrate interface, respectively. All images are taken viewed along ⟨110⟩ because, along this direction, columns of pure Ho and pure Ti, as well as mixed Ho/Ti columns, can be observed. The characteristic atomic column intensity profiles along two different directions, i.e., across Ho-Ti columns (I) and across Ho-Ho/Ti columns (II), for the single-crystal sample are shown in the inset in Fig. 5(a), i.e., the pure Ho ($Z = 67$) columns have a much larger intensity compared to the pure Ti ($Z = 22$) columns.

From the images taken on the (110) film, we can easily identify that the film has antiphase boundaries (APBs), typical of those found in pyrochlore structures [60]; these are very likely growth defects. In Fig. 5(d), we show the atomic column intensity profiles for the (110) film for the two different regions that were studied. Away from the substrate interface [Fig. 5(b)], we present the profiles for a (111) APB [top
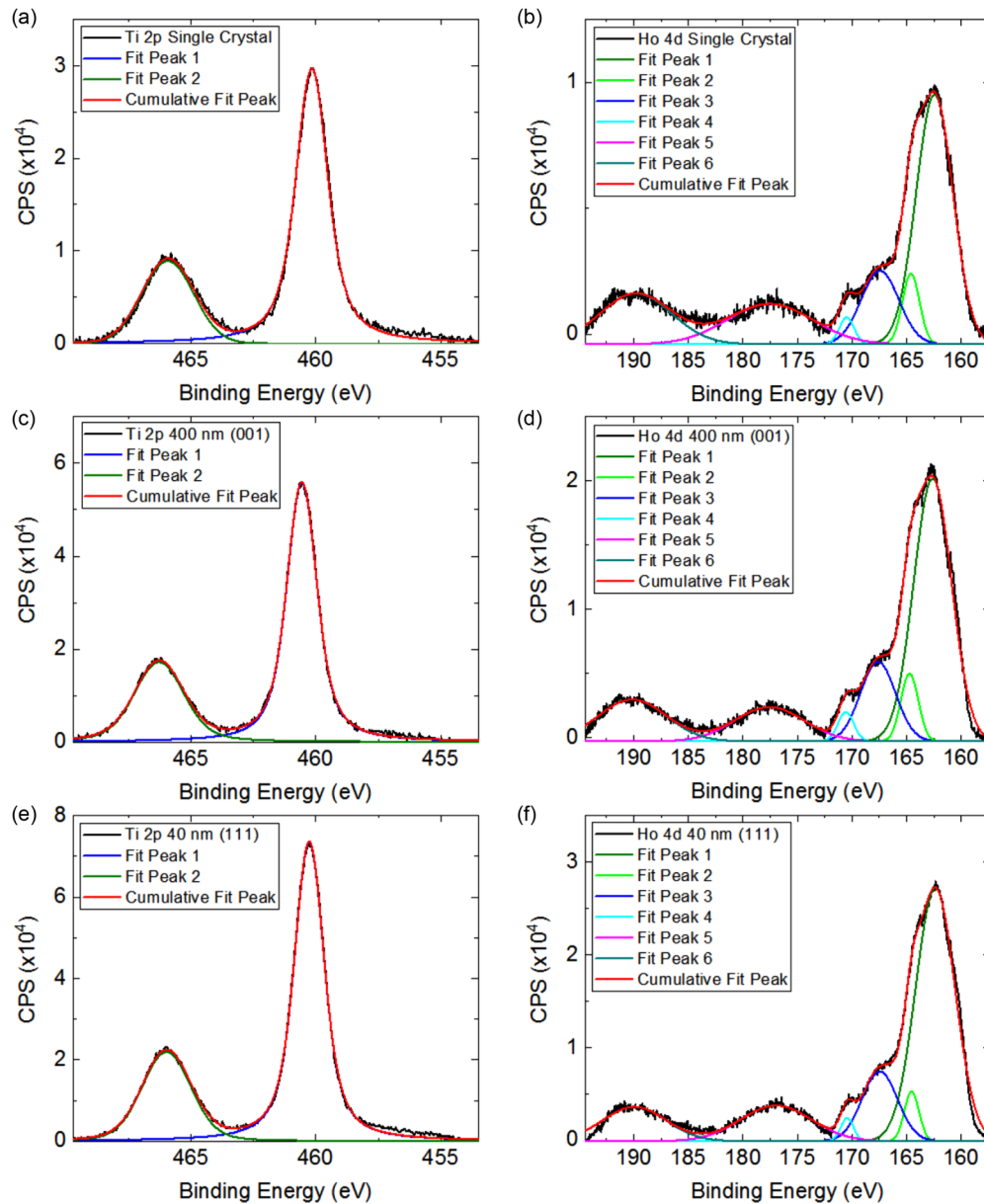
FIG. 4. XPS spectra of Ti 2p peaks and Ho 4d peaks for a Ho$_2$Ti$_2$O$_7$ single crystal, a 400 nm (001) thin film, and a 40 nm (111) thin film. (a) Ti 2p region of the single crystal. (b) Ho 4d region of the single crystal. (c) Ti 2p region of the 400 nm (001) thin film. (d) Ho 4d region of the 400 nm (001) thin film. (e) Ti 2p region of the 40 nm (111) thin film. (f) Ho 4d region of the 40 nm (111) thin film. The best fits for each set of spectra are displayed along with the baseline subtracted data from the actual scan. For more details on baseline subtraction, see the Supplemental Material [45].

panels in Fig. 5(d), across Ho-Ho/Ti and Ti-Ho/Ti columns] and for a "perfect area" [center panel in Fig. 5(d), across Ho-Ti columns and across Ho-Ho/Ti columns]. The profiles of the perfect area show intensities very comparable to the single crystal, clearly showing that a large region of the (110) film shows a crystallinity and stoichiometry expected for pristine Ho$_2$Ti$_2$O$_7$. Figure 5(c) shows a region close to the YSZ substrate. Two profiles (I and II, both taken across Ho-Ti columns) are presented in the bottom panel of Fig. 5(d). There is little intensity difference between Ho and Ti columns along one [110] direction, unlike the alternating intensity of the perfect area (center panel). This indicates that in addition

to the APBs, there is a clear presence of antisite disorder, as illustrated by the intensity variations of the pure Ho and Ti columns (see red arrows) in Fig. 5(d), bottom panel. In the intensity line profile I (across Ho-Ti columns), one Ho column has lower intensity than the adjacent Ho columns, indicating quite a few Ti went into this column and, vice versa, the two Ti columns have higher intensity, implying Ho went into the Ti columns in line profile II. We have repeated a similar study regarding APBs and antisite disorder on a (111) and on a (001) film, which we present in the Supplemental Material [45]. A comparison of the three films to the single crystal clearly indicates that the films have APBs and antisite disorder, but
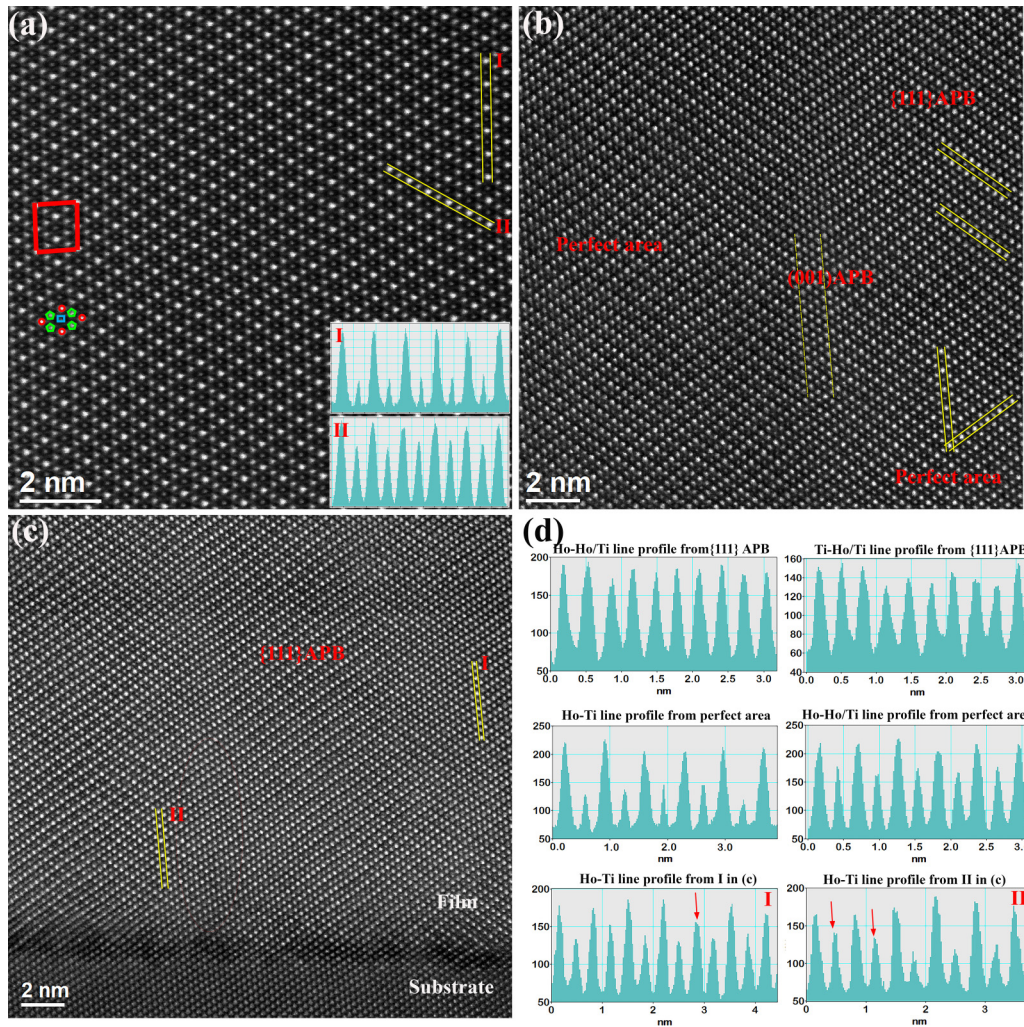
FIG. 5. (a) HAADF-STEM image of an $Ho_2Ti_2O_7$ single crystal along [110]. The unit cell is delineated with a red rectangle. Pure Ho atomic column indicated by red circle; Ho/Ti mixed column indicated by green polygon; pure Ti column indicated by blue rectangle. Insets: Intensity line profiles of Ho-Ti (I) and Ho-Ho/Ti (II) columns [x axis: 0–3.0 nm; y axis: intensity (arbitrary units)]. (b) HAADF-STEM image of the 118 nm (110) $Ho_2Ti_2O_7$ film collected away from the film/substrate interface. (c) HAADF-STEM image of the 118 nm (110) film at the film/substrate interface region. (d) Intensity line profiles from atomic columns indicated by yellow lines in (b) and (c). Top: Ho-Ho/Ti and Ti-Ho/Ti line profiles from (111) APB of (b); middle: Ho-Ti and Ho-Ho/Ti line profiles from perfect area in film of (b); bottom: Ho-Ti line profiles from (c) showing antisites disorder. Red arrow indicates Ti into Ho sites in (I) and Ho into Ti sites in (II).

the TEM data show no evidence of an appreciable amount of stuffing, i.e., additional Ho on the Ti site.

A series of neutron-scattering measurements has been performed on (111) $Ho_2Ti_2O_7$ thin films with thicknesses ranging from 40 to 400 nm [see Fig. 2(b) for the evolution of d spacing with increasing film thickness] using the MACS and SPINS instruments at the NCNR. Schematic representations of the scattering map and the corresponding magnetic structure of the $Ho_2Ti_2O_7$ unit cell are depicted in Figs. 6(a) and 6(b). Figure 6(c) shows a scattering map of the scattering intensity of the (hhl) plane of the 400 nm film taken at $T = 0.1$ K on MACS after field cooling the film in a 5 T field (applied along the [$1\bar{1}0$] direction). Data taken at 25 K and 0 T are used as background and subtracted to more clearly show the magnetic contribution. With the field applied along the [$1\bar{1}0$] direction of $Ho_2Ti_2O_7$, as described in [12], the spin system is separated into two sets of chains, i.e., parallel to the field (α

chains) and perpendicular to the field (β chains) [see Figs. 1(a) and 6(b)]. The β chains can either be parallel or antiparallel to one another. The parallel case gives scattering intensity at $Q = 0$, while the antiparallel case, associated with a symmetry lowering, will result in scattering intensity at the $Q = 0$ and the $Q = X$ positions [see Figs. 6(a) and 6(b)], with zone boundary peaks reportedly increasing in intensity in applied fields [11].

In the scattering map presented in Fig. 6(c), the intensity near the ($22\bar{2}$) position is due to the ($11\bar{1}$) and (111) YSZ structural reflections, respectively. The scattering intensities at the ($\bar{1}\bar{1}3$), ($11\bar{3}$), (111), and ($\bar{1}\bar{1}\bar{1}$) positions are from the film and consist of both structural and magnetic contributions. The magnetic component of each peak is strongly dependent on the applied field as evidenced by the dramatic enhancement of their respective intensities when a magnetic field is applied; hence, the strong field dependence is attributed to
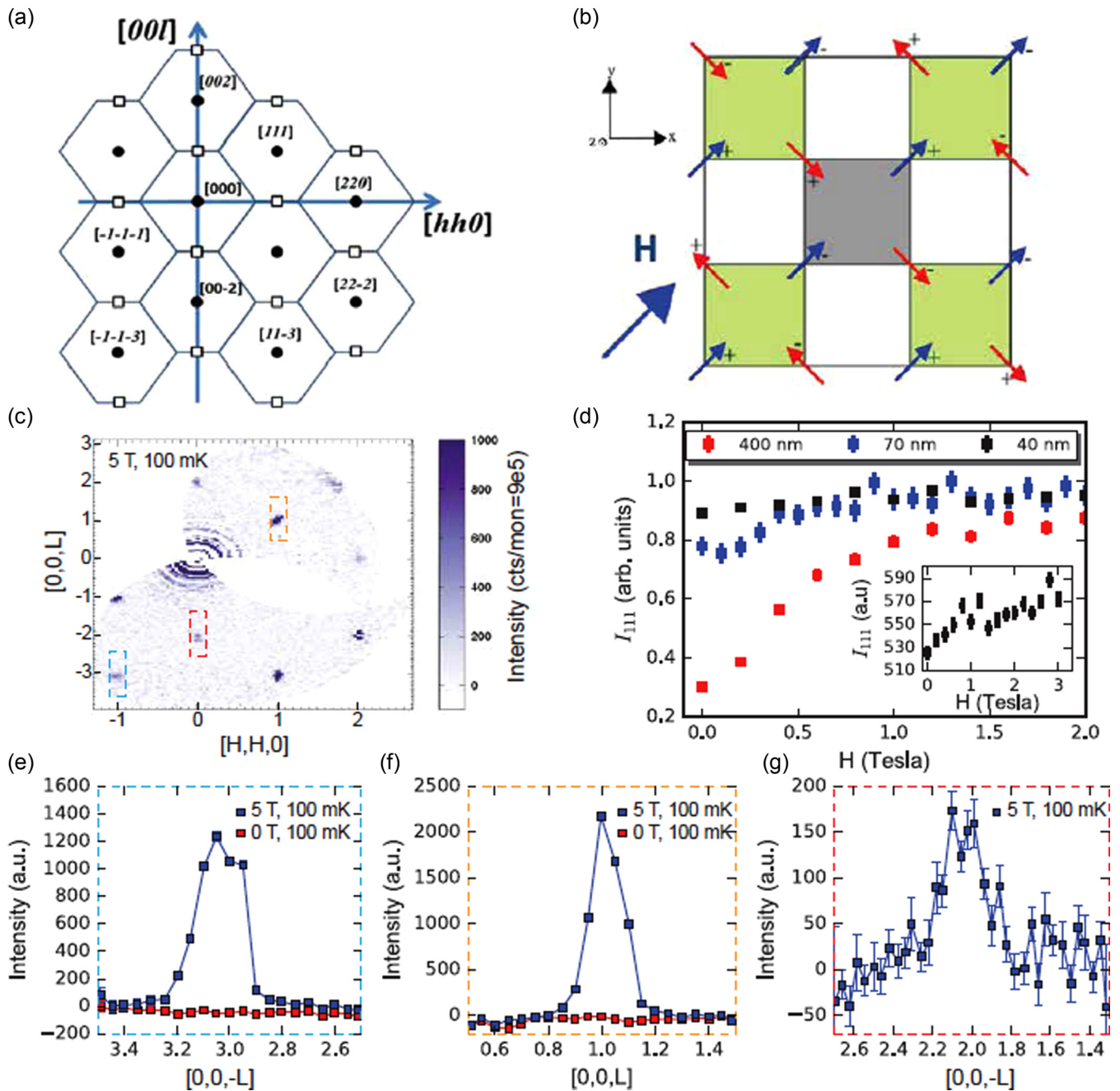
FIG. 6. (a) A representation of the reciprocal space map for the pyrochlore lattice. The full circles show the positions of Bragg peaks for a $Q = 0$ (zone center) magnetic structure, while the open squares show the $Q = X$ positions (zone boundary) [12]. (b) The $Ho_2Ti_2O_7$ unit cell projected down the z axis. The component of each spin that is parallel to the z axis is designated by the $+$ and $-$ signs. The four tetrahedra that make up the unit cell appear as the light-green squares. The gray square in the middle is not a tetrahedron, but its diagonally opposite spins inhabit the same lattice plane. The schematic depicts the $Q = X$ magnetic structure [antiparallel β chains (red) and polarized α chains (blue)]. The large arrow along the [110] direction indicates the direction of the applied magnetic field. (c) Map of the scattering intensity of the (hhl) plane of a 400-nm-thick $Ho_2Ti_2O_7$ sample grown on (111) YSZ after field cooling the sample to $T = 0.1$ K in $H = 5$ T applied along the [1-10] direction (in-plane) of the film. To obtain this map, the scattering intensity at $T = 25$ K and $H = 0$ T was subtracted as background. (d) Integrated intensity of the [111] magnetic film peak as a function of applied field at $T = 100$ mK for a 400-, 70-, and 40-nm-thick (111) film normalized to the intensity at 2 T. Inset: Unnormalized data from the 40 nm film to illustrate the small intensity increase with field. For these neutron measurements, all error bars and confidence intervals are given by standard deviations of the Poisson distribution. Cuts taken along the (00l) direction through the (e) ($\bar{1}\bar{1}\bar{3}$) and (f) (111) reciprocal space positions integrated along (hh0) from (0.9 0.9 l) to (1.1 1.1 l) at 100 mK and 5 T (blue) for the data in (c) and for an equivalent data set taken at 100 mK and 0 T (red). The zero-field data set has the same 25 K and 0 T data set subtracted as background. (g) Cut taken along the (00l) direction through the (00$\bar{2}$) reciprocal space position integrated along (hh0) from (-0.15 -0.15 l) to (0.15 0.15 l) for the background-subtracted data set in (c).

the magnetic order in the bulk of the film associated with the polarized state. Figure 6(d) shows the scattering intensity of the (111) film reflection as a function of applied field for films of varying thickness taken on SPINS. The data are normalized by the intensity measured at 2 T. The results indicate that the films saturate into the high-polarized state under applied fields and that lower saturation fields are needed for the thinner films. The intensity at the (002) and (00$\bar{2}$) film positions only shows up under applied field (consistent with the fact that these peaks are structurally forbidden). Figures 6(e) and 6(f) show cuts along the (00l) direction through the ($\bar{1}\bar{1}3$) and (111) reciprocal space positions, respectively, integrated from (0.9 0.9 l) to (1.1 1.1 l) at 100 mK at 0 T (red) and at 5 T (blue), with the same 25 K and 0 T scans subtracted as background. Figure 6(g) shows the same cut through the subtracted (00$\bar{2}$) at 100 mK and 5 T. These illustrate the dramatic magnetic enhancement at these reflections, as we see no difference for the film nuclear peaks from 25 to 0.1 K in zero field (i.e., no peak), but see clear peaks when the field is applied. The (002)-like reflections in particular are not visible at all in the unmagnetized state, indicating that these peaks are magnetic in origin.

To summarize, the presence of only the (113)-, (111)-, and (002)-like film peaks, i.e., $Q = 0$, after field cooling the film in a 5 T field, and the absence of scattering at the $Q = X$ positions, indicate that the 400 nm film only shows parallel β chains and polarized α chains [see Fig. 6(b)]. However, the absence of scattering at these positions could be a result of substrate background issues that hinder the observation of diffuse scattering. Important to note is that the appearance of the (002) is consistent with the $Q = 0$ magnetic structure as previously reported [11,12,61].

Next, we investigate the anisotropy in each of the films by discussing the magnetization as a function of applied field measured at 1.8 K (see Fig. 7). It is important to emphasize that all MPMS measurements were performed with the field along the indicated crystallographic directions with a precision of about 2° (see Supplemental Material for further details [45]). In Fig. 7(a), the magnetization is shown for a 85-nm-thick film grown on (001) YSZ with the field applied along the [100] in-plane direction (dotted curve), the [001] direction (along the film normal, dashed curve), and along the [111] direction (54.7° from the film normal). The horizontal dashed lines indicate the expected saturation magnetization values obtained from simulations of the dipolar spin-ice model when the field is applied along each of the different crystallographic directions of the sample ($\mu = 10$ μ_B/Ho) [33]. We find that for H $||\langle100\rangle$ and H $||$ [111], the film shows the expected $M = 5.8$ and 5 μ_B/Ho, respectively. Comparing the responses when H $||$ [001] and H $||$ [100], it is clear that the film saturates at significantly lower fields when the field is applied in the film plane. This shows that the geometric anisotropy intrinsic to the film may play a role in the modification of spin-ice physics. The observed slow saturation of the film when H $||$ [111], which has a significant component along the film normal, may be a result of the same shape effect and likely plays a role in obscuring the magnetization plateau. The effect of shape anisotropy on the magnetic properties of Ho$_2$Ti$_2$O$_7$ thin films is also evident from temperature-
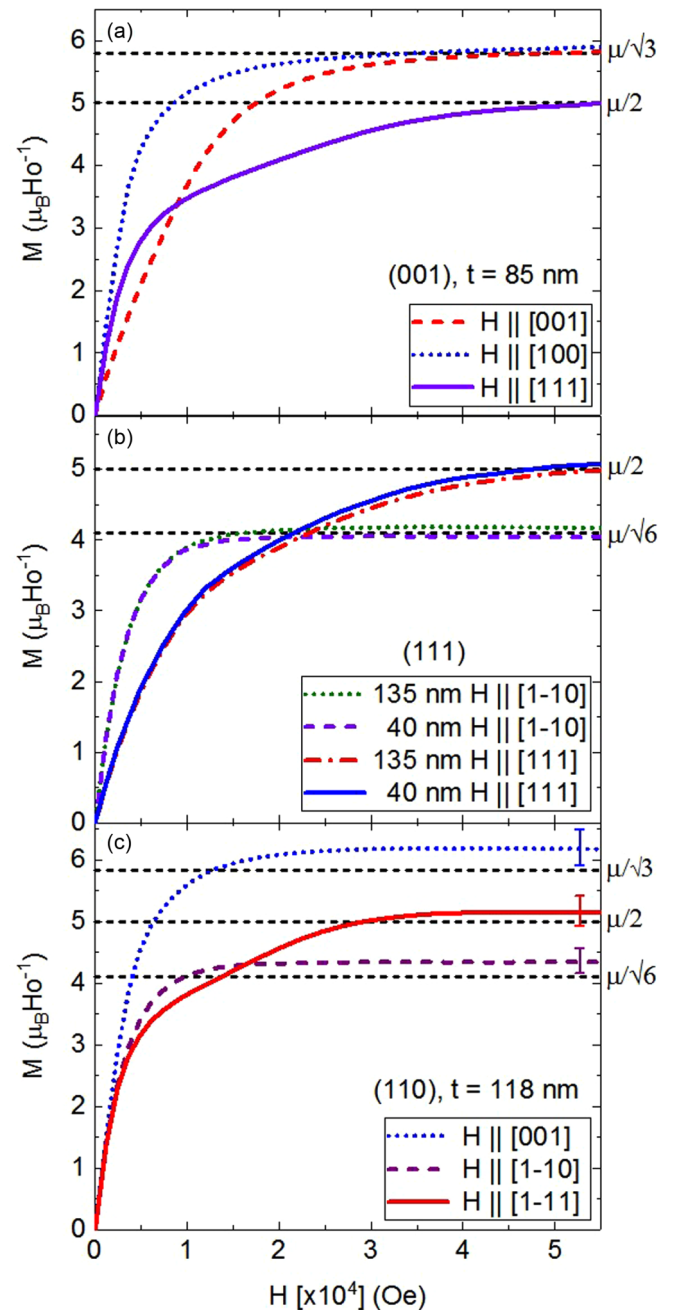

FIG. 7. Magnetization plotted as a function of applied field (a) For a 85-nm-thick (001) thin film with H applied along the [001] (out-of-plane), [100] (in-plane), and [111] (54.7° from the film normal) directions. (b) For a 135-nm- and a 40-nm-thick (111) thin film with H applied along the [111] (out-of-plane) and [1$\bar{1}$0] (in-plane) directions. (c) For a 118-nm-thick (110) thin film with the field applied along the [001], [1$\bar{1}$0], and [1$\bar{1}$1] in-plane directions. The error bars (±5%) on each curve are a result of the error in the fitted thickness from the x-ray reflectivity results (see Supplemental Material [45]) and are representative of the error bars for the (111) and (001) samples as well. The expected values for the saturation magnetization from simulations of the dipolar spin-ice model are displayed as the black dashed horizontal lines in each figure ($\mu = 10$ μ_B/Ho, μ_B/Ho = 927.4×10^{-26} J T^{-1}/Ho). All measurements were performed at $T = 1.8$ K. The curves are corrected for their individual substrate contributions.

dependent susceptibility measurements. Below 10 K, the temperature-dependent magnetization shows a clear linear regime observed only for in-plane directions, very similar to observations by others in single crystals [22], while a more parabolic shape is observed for out-of-plane directions (see Supplemental Material for more details [45]).

In Fig. 7(b), the magnetization is shown for a 40 nm and a 135 nm thin film grown on a (111) YSZ substrate. For each film, data are shown for the field applied along the [111] out-of-plane direction and for the [1$\bar{1}$0] in-plane direction. We find that the saturation magnetization values correspond to the expected values for bulk (for H ||[1$\bar{1}$0], $M = 4.1$ μ_B/Ho). For this orientation, we again find that the films have a hard time saturating when the field is applied in the out-of-plane direction. For these (111) films, there is no evidence of a plateau state. While shape anisotropy may play a role in how easily the films are saturated, interestingly, no thickness dependence is observed in the magnetization measurements; the 40 nm film, in which the strained layer makes up a significant portion of the film, and the 135 as well as the 400 nm films, which are mostly relaxed, show magnetization curves that are virtually indistinguishable (see Supplemental Material [45]). This lack of thickness dependence and the lack of a plateau state have been observed for both (001) and (111) films (see Supplemental Material for more details [45]).

In Fig. 7(c), we show the response for a 118 nm (110) film, which has the [111] direction in the plane of the film. Here measurements with H || [001], [1$\bar{1}$0], and [1$\bar{1}$1] are all in-plane directions and saturate rapidly with increasing field in a way very similar to bulk observations [20,33]. The error bars on each curve are a result of the error in the fitted thickness from the x-ray reflectivity measurements collected for the sample. This error encompasses a ±5% range around the fitted values and is representative of the error expected for the other samples grown on (111) and (001) substrates as well. Although the plateau state is quite weak at this temperature (1.8 K), it is clearly visible for the [111] direction in this film.

To further highlight the presence of the plateau state in the (110) film, we present the derivatives ($\frac{dM}{dH}$) of all four films with H || [111] in Fig. 8(a). For comparison, we also show the derivative of a measurement performed on a single crystal. The development of an intermediate plateau at around 3.33 μ_B/Ho, with the onset of a magnetic transition and saturation to around 5.0 μ_B/Ho, is clearly visible in our single crystal, consistent with reports by others [15,20,34,35] and with expectations from Monte Carlo simulations of the dipolar spin-ice model [33]. For the single crystal, we have investigated the effect of misalignment of the field with the [111] direction. Magnetization vs field curves for a single crystal, in which we purposely misaligned the field away from the [111] direction by 4° (both toward the [110] and [001] directions) and by 10° (towards the [001]), show that misalignment of well over 4° is needed to significantly diminish the plateau. Note that the crystal was measured using the same system and alignment procedure as is used for the films. Furthermore, we find that the plateau in the single crystal diminishes quickly as the temperature is increased from 1.8 to 3 K (see Supplemental Material for more details [45] on the temperature dependence and the misalignment study). To confirm the disappearance of the plateau with increased
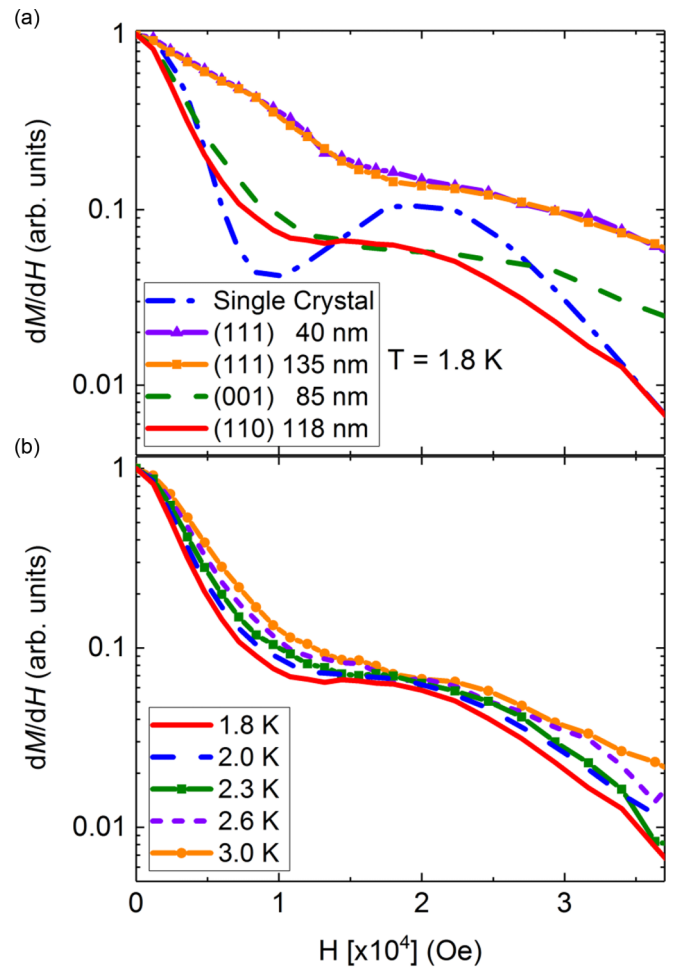

FIG. 8. (a) Derivative dM/dH as a function of applied field along the [111] direction for films grown on (001) YSZ, (110) YSZ, and (111) YSZ. The measurement of a single crystal with H || [111] is displayed for comparison. All measurements were performed at $T = 1.8$ K. (b) Derivative dM/dH as a function of temperature for the (110) film with H || [111]. The vertical axis in each figure has been normalized and is plotted on a logarithmic scale to highlight the presence of a plateau in M vs H.

temperature, we show a temperature-dependent study of the (110) thin-film plateau state in Fig. 8(b), which clearly shows that the plateau disappears when the temperature is increased by about 1 K. Based on these results, misalignment in the measurement can effectively be ruled out as a cause for the smudged plateau in the (110) thin film. Therefore, we could conclude that the spin-ice physics is modified in the films, leading to slight suppression of the temperature at which the spin-ice state gets locked in.

Based on the results presented here, it is clear that the spin-ice state is perturbed in our thin films, which is due to the strained unit cell and disorder in the form of antisites. It is interesting to compare our results to those presented by others. Leusink *et al.* [36] report on $Ho_2Ti_2O_7$ films grown on YSZ substrates, with magnetization measurements showing the expected anisotropy and the hallmark plateau for films grown on (110) YSZ, indicating that the spin-ice physics was preserved in their films. In our films, the plateau state is smudged due

to the presence of antisites and a distorted unit cell. In Bovo *et al.* [32], magnetization measurements on $Dy_2Ti_2O_7$ thin films show the presence of the expected magnetic anisotropy of the spin-ice state. Furthermore, based on temperature-dependent susceptibility and specific-heat measurements, the spin-ice state in those films was reportedly perturbed due to a strain-induced structural distortion, leading to an estimated change in nearest-neighbor superexchange interaction ΔJ_{nn} of $\sim$0.1 K. Thus, for comparison, we used our lattice parameters determined from x-ray diffraction and TEM measurements to estimate rough values of ΔJ_{nn} for our films (see Supplemental Material for more details [45]). The obtained values in our films range from 0.02 to 0.1 K. Direct comparisons between the values for ΔJ_{nn} would lead to the conclusion that the spin-ice state in our films is exposed to a perturbation of similar magnitude as in Ref. [32]. While it is possible that the third law is also restored in our films, it is unclear how antisite disorder and APBs would affect this; it would be interesting to attempt specific-heat measurements in the future to probe the effect of disorder on the residual entropy.

IV. CONCLUSIONS

We have grown high-quality epitaxial thin films of the pyrochlore titanate $Ho_2Ti_2O_7$ and find that the orientation of the substrate plays a key role in determining the strain state and the relaxation rate of the films. Elastic neutron-scattering experiments on (111) films clearly showed the presence of the $Q = 0$ phase in films of varying thickness, but observation of the $Q = X$ phase (the plateau state in magnetization measurements) in the films remains elusive. XRD and TEM measurements show that our films have an enlarged unit cell compared to the expected 10.1 Å. The TEM measurements show that appreciable stuffing is not present, but there is a clear presence of antisite disorder and APBs in the films. The increased lattice parameters are likely due to strain and the disorder in the films. Magnetization measurements further support that we have stoichiometric $Ho_2Ti_2O_7$. In our extensive magnetization studies, we find a diminished, but

clearly observable plateau for the (110) film (i.e., when the [111] direction is an in-plane direction) and an absence of the plateau states in the (001) and (111) films. It is unlikely that misalignment is responsible for the absence of the plateau states in these orientations. We find that for the single crystal, a misalignment of well over $4°$ is necessary to start losing the plateau. Looking at the similarities between the single-crystal M vs H measurement at 3 K and our thin-film measurement at 1.8 K for the (110) film, it seems plausible that the diminishing of the plateau is due to a suppression of the temperature at which correlations drive the system into the spin-ice state. This suppression is likely due to the presence of defects in the films and perhaps the slightly larger separation of the Ho ions in the films due to the inflated unit cell.

[1] A. P. Ramirez, Annu. Rev. Mater. Sci. **24**, 453 (1994).

[2] C. L. Henley, Annu. Rev. Condens. Matter Phys. **1**, 179 (2010).

[3] S. Powell, Phys. Rev. B **91**, 094431 (2015).

[4] T. Fennell, P. P. Deen, A. R. Wildes, K. Schmalzl, D. Prabhakaran, A. T. Boothroyd, R. J. Aldus, D. F. McMorrow, and S. T. Bramwell, Science **326**, 415 (2009).

[5] M. J. P. Gingras and P. A. McClarty, Rep. Prog. Phys. **77**, 056501 (2014).

[6] C. Castelnovo, R. Moessner, and S. L. Sondhi, Nature (London) **451**, 42 (2008).

[7] L. D. C. Jaubert and P. C. W. Holdsworth, J. Phys.: Condens. Matter **23**, 164222 (2011).

[8] H. Cao, A. Gukasov, I. Mirebeau, P. Bonville, C. Decorse, and G. Dhalenne, Phys. Rev. Lett. **103**, 056402 (2009).

[9] B. Tomasello, C. Castelnovo, R. Moessner, and J. Quintanilla, Phys. Rev. B **92**, 155120 (2015).

[10] J. S. Gardner, M. J. P. Gingras, and J. E. Greedan, Rev. Mod. Phys. **82**, 53 (2010).

[11] J. P. Clancy, J. P. C. Ruff, S. R. Dunsiger, Y. Zhao, H. A. Dabkowska, J. S. Gardner, Y. Qiu, J. R. D. Copley, T. Jenkins, and B. D. Gaulin, Phys. Rev. B **79**, 014408 (2009).

[12] M. J. Harris, S. T. Bramwell, D. F. McMorrow, T. Zeiske, and K. W. Godfrey, Phys. Rev. Lett. **79**, 2554 (1997).

[13] M. Harris, S. Bramwell, T. Zeiske, D. McMorrow, and P. King, J. Magn. Magn. Mater. **177–181**, 757 (1998).

[14] L. Bovo, L. D. C. Jaubert, P. C. W. Holdsworth, and S. T. Bramwell, J. Phys.: Condens. Matter **25**, 386002 (2013).

[15] A. L. Cornelius and J. S. Gardner, Phys. Rev. B **64**, 060406(R) (2001).

[16] S. T. Bramwell, M. J. Harris, B. C. den Hertog, M. J. P. Gingras, J. S. Gardner, D. F. McMorrow, A. R. Wildes, A. L. Cornelius, J. D. M. Champion, R. G. Melko, and T. Fennell, Phys. Rev. Lett. **87**, 047205 (2001).

[17] G. Ehlers, A. L. Cornelius, M. Orendáč, M. Kajnaková, T. Fennell, S. T. Bramwell, and J. S. Gardner, J. Phys.: Condens. Matter **15**, L9 (2003).

[18] L. Pauling, J. Am. Chem. Soc. **57**, 2680 (1935).

[19] L. Pauling, *The Nature of the Chemical Bond and the Structure of Molecules and Crystals: An Introduction to Modern Structural Chemistry*, George Fisher Baker Non-Resident Lecture Series (Cornell University Press, Cornell, 1960).

[20] C. Krey, S. Legl, S. R. Dunsiger, M. Meven, J. S. Gardner, J. M. Roper, and C. Pfleiderer, Phys. Rev. Lett. **108**, 257204 (2012).

[21] B. C. den Hertog and M. J. P. Gingras, Phys. Rev. Lett. **84**, 3430 (2000).

[22] R. Siddharthan, B. S. Shastry, A. P. Ramirez, A. Hayashi, R. J. Cava, and S. Rosenkranz, Phys. Rev. Lett. **83**, 1854 (1999).

[23] H. D. Zhou, J. G. Cheng, A. M. Hallas, C. R. Wiebe, G. Li, L. Balicas, J. S. Zhou, J. B. Goodenough, J. S. Gardner, and E. S. Choi, Phys. Rev. Lett. **108**, 207206 (2012).

[24] C. R. Wiebe and A. M. Hallas, APL Mater. **3**, 041519 (2015).

[25] S. T. Bramwell and M. J. P. Gingras, Science **294**, 1495 (2001).

[26] H. D. Zhou, S. T. Bramwell, J. G. Cheng, C. R. Wiebe, G. Li, L. Balicas, J. A. Bloxsom, H. J. Silverstein, J. S. Zhou, J. B. Goodenough, and J. S. Gardner, Nat. Commun. **2**, 478 (2011).

[27] L. D. C. Jaubert, J. T. Chalker, P. C. W. Holdsworth, and R. Moessner, Phys. Rev. Lett. **105**, 087201 (2010).

[28] M. Mito, S. Kuwabara, K. Matsuhira, H. Deguchi, S. Takagi, and Z. Hiroi, J. Magn. Magn. Mater. **310**, e432 (2007).

[29] J. Röchner, L. Balents, and K. P. Schmidt, Phys. Rev. B **94**, 201111(R) (2016).

[30] L. D. C. Jaubert, T. Lin, T. S. Opel, P. C. W. Holdsworth, and M. J. P. Gingras, Phys. Rev. Lett. **118**, 207206 (2017).

[31] E. Lantagne-Hurtubise, J. G. Rau, and M. J. P. Gingras, Phys. Rev. X **8**, 021053 (2018).

[32] L. Bovo, X. Moya, D. Prabhakaran, Y.-A. Soh, A. T. Boothroyd, N. D. Mathur, G. Aeppli, and S. T. Bramwell, Nat. Commun. **5**, 3439 (2014).

[33] R. G. Melko and M. J. P. Gingras, J. Phys.: Condens. Matter **16**, R1277 (2004).

[34] O. A. Petrenko, M. R. Lees, and G. Balakrishnan, Phys. Rev. B **68**, 012406 (2003).

[35] H. Fukazawa, R. G. Melko, R. Higashinaka, Y. Maeno, and M. J. P. Gingras, Phys. Rev. B **65**, 054410 (2002).

[36] D. P. Leusink, F. Coneri, M. Hoek, S. Turner, H. Idrissi, G. V. Tendeloo, and H. Hilgenkamp, APL Mater. **2**, 032101 (2014).

[37] J. M. Farmer, L. A. Boatner, B. C. Chakoumakos, M.-H. Du, M. J. Lance, C. J. Rawn, and J. C. Bryan, J. Alloys Compd. **605**, 63 (2014).

[38] G. Ehlers, E. Mamontov, M. Zamponi, A. Faraone, Y. Qiu, A. L. Cornelius, C. H. Booth, K. C. Kam, R. L. Toquin, A. K. Cheetham, and J. S. Gardner, J. Phys.: Condens. Matter **20**, 235206 (2008).

[39] G. Lau, B. Muegge, T. McQueen, E. Duncan, and R. Cava, J. Solid State Chem. **179**, 3126 (2006).

[40] G. Lau, T. McQueen, Q. Huang, H. Zandbergen, and R. Cava, J. Solid State Chem. **181**, 45 (2008).

[41] B. G. Ueland, G. C. Lau, R. S. Freitas, J. Snyder, M. L. Dahlberg, B. D. Muegge, E. L. Duncan, R. J. Cava, and P. Schiffer, Phys. Rev. B **77**, 144412 (2008).

[42] G. C. Lau, R. S. Freitas, B. G. Ueland, M. L. Dahlberg, Q. Huang, H. W. Zandbergen, P. Schiffer, and R. J. Cava, Phys. Rev. B **76**, 054430 (2007).

[43] H. D. Zhou, C. R. Wiebe, Y. J. Jo, L. Balicas, Y. Qiu, J. R. D. Copley, G. Ehlers, P. Fouquet, and J. S. Gardner, J. Phys.: Condens. Matter **19**, 342201 (2007).

[44] K. E. Arpino, B. A. Trump, A. O. Scheie, T. M. McQueen, and S. M. Koohpayeh, Phys. Rev. B **95**, 094407 (2017).

[45] See Supplemental Material at http://link.aps.org/supplemental/10.1103/PhysRevMaterials.3.084412 for the AFM measurements, thickness determination from fitting x-ray reflectivity (xrr) measurements, the SAED patterns, additional RSMs, and additional magnetization vs field curves measured at various temperatures for the single crystal.

[46] The identification of any commercial product or trade names does not imply endorsement or recommendation by the National Institute of Standards and Technology.

[47] M. Björck and G. Andersson, J. Appl. Crystallogr. **40**, 1174 (2007).

[48] J. A. Rodriguez, D. M. Adler, P. C. Brand, C. Broholm, J. C. Cook, C. Brocker, R. Hammond, Z. Huang, P. Hundertmark, J. W. Lynn, N. C. Maliszewskyj, J. Moyer, J. Orndorff, D. Pierce, T. D. Pike, G. Scharfstein, S. A. Smee, and R. Vilaseca, Meas. Sci. Technol. **19**, 034023 (2008).

[49] R. Azuah, L. Kneller, Y. Qiu, P. Tregenna-Piggott, C. Brown, J. Copley, and R. Dimeo, J. Res. Natl. Inst. Stand. Technol. **114**, 341 (2009).

[50] M. Yashima, S. Sasaki, M. Kakihana, Y. Yamaguchi, H. Arashi, and M. Yoshimura, Acta Cryst. **B50**, 663 (1994).

[51] M. B. Pomfret, C. Stoltz, B. Varughese, and R. A. Walker, Anal. Chem. **77**, 1791 (2005).

[52] S. Simson, N. Heide, and J. W. Schultze, Surf. Interface Anal. **22**, 431 (1994).

[53] E. McCafferty and J. P. Wightman, Surf. Interface Anal. **26**, 549 (1998).

[54] B. Erdem, R. A. Hunsicker, G. Simmons, D. Sudol, V. L. Dimonie, and M. El-Aasser, Langmuir **17**, 2664 (2001).

[55] V. Bukauskas, S. Kaciulis, A. Mezzi, A. Mironas, G. Niaura, M. Rudzikas, I. Šimkienė, and A. Šetkus, Thin Solid Films **585**, 5 (2015).

[56] H. Ogasawara, A. Kotani, and B. T. Thole, Phys. Rev. B: Condens. Matter **50**, 12332 (1994).

[57] W. C. Lang, B. D. Padalia, L. M. Watson, D. J. Fabian, and P. R. Norris, Faraday Discuss. Chem. Soc. **60**, 37 (1975).

[58] Y. A. Teterin and A. Y. Teterin, Russ. Chem. Rev. **71**, 347 (2002).

[59] B. D. Padalia, W. C. Lang, P. R. Norris, L. M. Watson, and D. J. Fabian, Proc. R. Soc. London, Ser. A **354**, 269 (1977).

[60] Z. Shafieizadeh, Y. Xin, S. M. Koohpayeh, Q. Huang, and H. D. Zhou, Sci. Rep. **8**, 17202 (2018).

[61] T. Fennell, O. A. Petrenko, B. Fåk, J. S. Gardner, S. T. Bramwell, and B. Ouladdiaf, Phys. Rev. B **72**, 224411 (2005).